Platform and Environmental Effects on Above-Water Determinations of Water-Leaving Radiances

STANFORD B. HOOKER

NASA Goddard Space Flight Center, Greenbelt, Maryland

ANDRÉ MOREL

Université Pierre et Marie Curie/CNRS, Villefranche-sur-Mer, France

(Manuscript received 26 September 2001, in final form 6 June 2002)

ABSTRACT

A comparison of above- and in-water spectral measurements in Case-1 conditions showed the uncertainty in above-water determinations of water-leaving radiances depended on the pointing angle of the above-water instruments with respect to the side of the ship. Two above-water data processing methods were used to create a diagnostic variable (formulated for Case-1 waters only) to quantify the presence of superstructure reflections that degraded the above-water intracomparisons of water-leaving radiances by as much as 13%–27% (for far-to-near viewing distances, respectively). The primary conclusions of the above- and in-water intercomparison of water-leaving radiances were as follows: (a) the SeaWiFS 5% radiometric objective was achieved with the in-water instruments; (b) the above-water approach produced agreement to within 5%, but reliably for about half the data, and only with well-controlled procedures and severe filtering to remove glint contamination; (c) a decrease in water-leaving radiance values was seen in the presence of swell, although, wave crests were radiometrically brighter than the troughs; and (d) standard band ratios used in ocean color algorithms remained severely affected, because of the relatively low signal at 555 nm and, thus, proportionally significant ship contamination at this wavelength. Suggestions for a more precise above-water measurement protocol are tentatively proposed.

1. Introduction

Ocean color satellite sensors (IOCCG 1998) provide large-scale synoptic observations of biogeochemical properties of the upper layer in the open ocean (e.g., phytoplankton biomass), as well as continuous monitoring of other important parameters in the coastal zones (e.g., sediment load and dissolved colored matter). This global capability is accomplished through the determination of radiometric quantities, specifically, the spectral values of the radiances at the top of the atmosphere from which (after atmospheric correction) the spectral radiances emerging from the ocean surface, $L_w(\lambda)$, are extracted (λ denotes the wavelength).

For meaningful applications, an extremely high radiometric accuracy is required. For example, the Sea-viewing Wide Field-of-view Sensor (SeaWiFS)[1] Project requires accuracies of 5% absolute and 1% relative in terms of the retrieved $L_w(\lambda)$ values (Hooker and Esaias 1993).[2] The first obvious condition for reaching such an accuracy lies in the conception and the realization of the spaceborne instrument. Although this is a necessary requirement, it is not sufficient to ensure the distributed radiometric data meet the accuracy objectives. Indeed, the success of any ocean color mission is determined in particular by the quality of the optical dataset collected for calibration and validation purposes, and involves several continuous activities (Hooker and McClain 2000): (a) characterizing and calibrating the sensor system, (b) analyzing trends and anomalies in the sensor performance and derived products (the L_w values and the chlorophyll concentration), (c) supporting the development and validation of algorithms (for the retrieval of bio-optical properties and for atmospheric correction), and (d) verifying the processing code and selecting ancillary data (e.g., ozone, wind, and atmospheric pressure) used in the data processing scheme.

This paper does not deal with all aspects of the calibration and validation process. It is restricted to those field measurements suitable for vicarious calibration, as

[1] See appendix A for glossary of terms.

[2] See appendix B for list of primary symbols.

Corresponding author address: Dr. Stanford B. Hooker, NASA GSFC, Code 970.2, Greenbelt, MD 20771.
E-mail: stan@ardbeg.gsfc.nasa.gov

well as the derivation or improvement of bio-optical algorithms. Historically, the fundamental radiometric quantities selected for comparison with the radiances measured by—or, more precisely, retrieved from—the spaceborne sensor were the upwelled spectral radiances just above the sea surface, $L_W(\lambda, 0^+)$ (the symbol 0^+ means immediately above the surface).

The $L_W(\lambda, 0^+)$ radiances can be derived by extrapolating in-water measurements taken close to the sea surface or obtained directly from above-water measurements. In-water techniques have been largely successful in Case-1 waters, but the above-water approach for vicarious calibration remains nevertheless attractive, because (a) the data can presumably be collected more rapidly and from a ship underway, and (b) the frequently turbid and strongly absorbing waters in shallow Case-2 environments impose severe limitations on in-water measurements, particularly because of the instrument self-shading effect. For both methods, protocols have been recommended (Mueller and Austin 1992) and revised (Mueller and Austin 1995; Mueller 2000a,b).

From a measurement perspective, the above-water problem is more restrictive, because presently there is no reliable mechanism for floating an above-water system away from a ship (which is easily and effectively accomplished for an in-water system), so all above-water measurements are made in close proximity to the vessel. The objective of the present study, based on high quality data collected during a one-month field campaign in Case-1 waters under excellent sky and sea-state conditions, is to compare both techniques in various geometrical conditions (pointing angles plus sun and ship positions), and to examine several problems associated with above-water determinations, particularly those caused by perturbations from the ship itself and other environmental factors, such as oceanic swell.

2. Theoretical framework

The basic equations relating the upward radiance field below the surface with that exiting the surface, the angular bidirectional dependency of these fields, and the transformation of radiance or irradiance into reflectance are detailed in Morel and Gentili (1996), Mobley (1999), and Mueller (2000a,b), so only the quantities needed here are briefly presented. The spectral radiance emerging from the ocean, the so-called water-leaving radiance, is the principal quantity of interest and is expressed as

$$L_W(\lambda, \theta, \phi \in \Omega_{\text{FOV}}, \theta_s, 0^+), \quad (1)$$

which explicitly shows the angular dependencies of L_W on the radiance direction defined by the zenith angle θ, and the azimuth angle with respect to the sun direction ϕ($\phi = 0$ for the sun's azimuth), and where Ω_{FOV} represents the solid angle of the detector centered on the direction (θ, ϕ). For a given detector, Ω_{FOV} is constant, and this argument is no longer repeated. The dependence on the illumination conditions prevailing above the sea surface is expressed in a simplified way by only introducing the solar zenith angle θ_s.

Immediately beneath the sea surface, at a null depth $z = 0^-$, the upwelled radiances denoted

$$L_u(\lambda, \theta', \phi, \theta_s, z), \quad (2)$$

where θ' is the nadir angle given by Snell's law according to $\theta' = \sin^{-1}(\sin\theta/n)$, and n is the refractive index of seawater. This radiance will be partly reflected (or totally reflected if θ' exceeds the critical angle), and partly transmitted through the interface in a direction θ (zenith angle), so that

$$L_W(\lambda, \theta, \phi, \theta_s, 0^+) = T(\theta')L_u(\lambda, \theta', \phi, \theta_s, 0^-), \quad (3)$$

and for which $T(\theta')$ is the (upward) radiance transmittance through the interface and equals $n^{-2}[1 - \rho(\theta')]$, where $\rho(\theta')$ is the (upward) Fresnel reflectance coefficient corresponding to the slant upward direction θ' (Austin 1974). The upward radiance is related to the upward irradiance E_u at the same depth (at 0^-, in this case), through

$$L_u(\lambda, \theta', \phi, \theta_s, 0^-) = \frac{E_u(\lambda, \theta_s, 0^-)}{Q(\lambda, \theta', \phi, \theta_s, 0^-)}, \quad (4)$$

where the dimensionless bidirectional Q function is expressed in steradians.

With an above-water method, the total radiance measured above the sea surface L_T includes the wanted information (L_W) plus a contamination term ΔL discussed later, originating from light reflected by the sea surface and into the sensor:

$$L_T(\lambda, \theta, \phi, \theta_s) = L_W(\lambda, \theta, \phi, \theta_s, 0^+) + \Delta L. \quad (5)$$

According to the latest version of the protocols (Mueller 2000a,b) and simulations by Mobley (1999), θ is usually chosen from 20° to 50° (here 40°), and ϕ is generally from 90° to 135° away from the sun's azimuth.

When using an in-water method, a vertical profile of L_u within the upper layer is determined with a radiometer pointed at nadir (θ' and $\phi = 0$). The $L_u(\lambda, 0, 0, \theta_s, 0^-)$ value at null depth is derived by extrapolating the profile toward the interface; it is then propagated through the interface using (3), with T given the value $T(\theta' = 0) = T_0 = 0.546$. The latter has a nearly constant value regardless of the sea state (Austin 1974), so that

$$L_W(\lambda, 0, 0, \theta_s, 0^+) = 0.546L_u(\lambda, 0, 0, \theta_s, 0^-). \quad (3')$$

By assuming the unwanted term, ΔL in (5), has been successfully removed, the problem is to meaningfully compare two determinations of L_W resulting from a simultaneous use of an above- and in-water method.

For in-water measurements, θ, θ', and ϕ are all zero, and Q in (4) takes a particular value, denoted $Q_n(\lambda, \theta_s, 0^-)$ (for the nadir viewing angle), which still depends on the sun position. For above-water measurements, the angular parameters θ', and ϕ in (4) are imposed by the pointing geometry of the sensor, and $T(\theta')$ differs slightly from (and actually is always less than) the T_0 value.

Making use of the superscripts ''abw'' and ''inw'' to represent the above- and in-water methods, respectively, the ratio of the L_W quantities is given by

$$\frac{L_W^{\text{abw}}}{L_W^{\text{inw}}} = \frac{T(\theta')}{T_0} \frac{Q_n(\lambda, \theta_s, 0^-)}{Q(\lambda, \theta', \phi, \theta_s, 0^-)}. \quad (6)$$

The remote sensing reflectance R_{rs} is defined as the ratio of the water-leaving radiance originating from nadir to the downward irradiance above the surface, $E_d(\lambda, \theta_s, 0^+)$:

$$R_{\text{rs}}(\lambda, \theta_s) = \frac{L_W(\lambda, 0, 0, \theta_s, 0^+)}{E_d(\lambda, \theta_s, 0^+)}, \quad (7)$$

so it can be easily derived from the in-water radiance measurement and an associated downward irradiance determination in air. When using the above-water determination, some manipulations, as indicated by (6), are needed to obtain R_{rs} from L_W^{abw}:

$$R_{\text{rs}}(\lambda, \theta_s) = \frac{L_W^{\text{abw}}(\lambda, \theta, \phi, \theta_s, 0^+)}{E_d(\lambda, \theta_s, 0^+)} \frac{Q(\lambda, \theta', \phi, \theta_s, 0^-)}{Q_n(\lambda, \theta_s, 0^-)} \frac{T_0}{T(\theta')}. \quad (8)$$

3. Background and goals

The SeaWiFS Project goal of determining water-leaving radiances to within 5% uncertainties has been well demonstrated for in-water measurements in Case-1 waters (Hooker and Maritorena 2000), but the uncertainties associated with above-water measurements have not been similarly assessed. This was the ultimate objective of the first SeaWiFS Bio-Optical Algorithm Round-Robin (SeaBOARR-98) experiment (Hooker et al. 1999). The majority of the data were collected over a short time period in shallow Case-2 waters, or close to the transition between Case-1 and Case-2 conditions, according to the threshold defined by Loisel and Morel (1998). The lack of measurements in unequivocally Case-1 waters was the primary motivation for extending the original activity to a deep ocean cruise.

a. The field campaign

The *Productivité des Systèmes Océaniques Pélagiques* (PROSOPE) cruise was designed to study the productivity of pelagic oceanic systems as a contribution to the Joint Global Ocean Flux Study (JGOFS)–France Program. The campaign was on board the research vessel *Thalassa* (74.5 m length, 13.9 m breadth, and 6.2 m draught), and started in Agadir, Morocco, on 4 September 1999 and ended in Toulon, France, on 4 October. The cruise track began with a detailed study (3 days) in the productive upwelling zone off the northwest African coast and ended within the much less productive Mediterrranean Sea waters (Fig. 1a). The latter included 5-day studies of an ultra-oligotrophic regime in the Eastern Mediterranean (southwest of Crete) and a mesotrophic site in the Ligurian Sea (northwest of Corsica). In between the long-duration sites, nine daily stations were sampled over 4-h periods centered around noon.

In addition to the usual determinations of JGOFS core parameters and other biochemical studies, extensive optical sampling was executed, particularly around and during the overpass of the SeaWiFS instrument. A part of this program was devoted to the upward radiance measurements, to the comparison of the above- and in-water methods, and to the evaluation of the difficulties associated with attaining the desired radiometric accuracy, specifically in the vicinity of a large sampling platform. One above-water and two in-water systems were used for these inquiries (Figs. 1b–1d, respectively): (a) the Low-Cost National Aeronautics and Space Administration (NASA) Environmental Sampling System (LoCNESS), (b) the SeaWiFS Free-Falling Advanced Light Level Sensors (SeaFALLS), and (c) the SeaWiFS Surface Acquisition System (SeaSAS).

The environmental conditions during the cruise were generally good, even exceptional in terms of sky condition and cloud cover, as well as in terms of the sea state and ambient wind (Table 1). The chlorophyll *a* data for the upper layer (everywhere Case-1 conditions) spanned two orders of magnitude (0.032–3.75 mg m^{-3}). The large range in chlorophyll *a* concentration, along with the diversity in optical measurements, makes the PROSOPE dataset well suited for investigating a variety of challenging bio-optical problems.

b. Objectives

The SeaBOARR-98 conclusions were based on three favorable days of useful data. From these data, four methods for correcting above-water observations intracompared at the 8% level, and they intercompared with three methods for processing the in-water data at the 9% level (Hooker et al. 2002a), although radiometric agreement at the 5% level was achieved in some circumstances. The methods selected for the PROSOPE cruise are a subset of SeaBOARR-98 and will be described later. Based on this previous experience, the optical sampling objectives for the PROSOPE cruise were as follows: (a) use two in-water profilers and one analysis method to compute $L_W(\lambda)$ from in-water data, (b) use one above-water measurement system, and two surface glint correction methods to compute $L_W(\lambda)$ from above-water data, and (c) use radiometers with a common calibration history to minimize intercalibration uncertainties. In addition, the PROSOPE analysis plan was designed to overcome some deficiencies acknowledged during the SeaBOARR-98 experiment and also included (i) intercomparing the above- and in-water methods in Case-1 waters and in deep ocean conditions, (ii) a correction scheme for the bidirectional effects at the sea surface, and (iii) identifying the origin, and quantifying the significance of, perturbations caused by the sampling

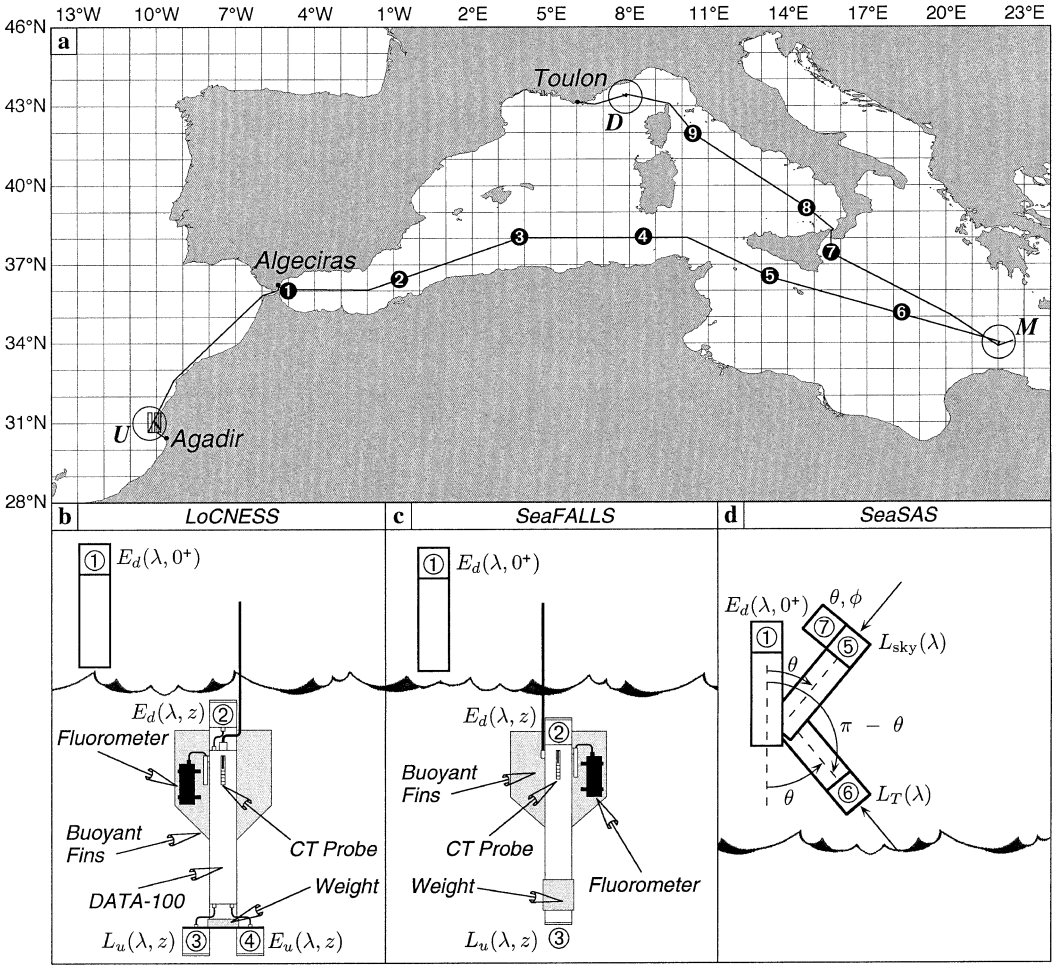

FIG. 1. A schematic of the PROSOPE cruise sampling: (a) the cruise track, with the short daily stations given by the (darkened) numbered bullets and the long multiday stations by the large circles (as encoded in Table 2); and the (b) LoCNESS, (c) SeaFALLS, and (d) SeaSAS instruments. For the latter, the (open) numerical bullets identify common sensor types. All three measurement systems were equipped with sensors to measure the vertical tilt φ of the radiometers during sampling.

platform and environmental conditions on the surface radiance field.

The magnitude of the perturbations in the proximity of a large structure is a recurring problem, which is made more complex according to the sun orientation with respect to the structure. These perturbations differentially influence the data obtained by the above- and in-water methods. For example, from the perspective of the in-water light field, investigations within 15–20 m of an offshore tower showed significant effects of the structure: approximately 3%–8% for clear-sky conditions, and as much as 20% under overcast conditions (Zibordi et al. 1999). Similar levels of uncertainties were estimated for in-water measurements from a ship (Voss et al. 1986).

For above-water measurements (recalling that the radiometer is never pointed into the ship's shadow), the perturbations are a combination of three possible effects: (a) the shadow cast by the vessel outside the field of view of the sensor, but within the attenuation pathlengths defined by the inherent water properties; (b) the interaction of the upward (in-water) radiant field with the submerged hull; and (c) the reflections off the sea surface from the interaction between the downward (above-water) radiant field and the exposed superstructure. The latter is expected to be the most important for above-water measurements, because the sun and sky are the light sources for the final perturbation and they are significantly more intense than the in-water radiant field (as shown later in Fig. 3).

4. Instrumentation and sampling procedures

All of the radiometers were built by Satlantic, Inc. (Halifax, Canada). Detailed descriptions of each instrument system have already been presented (Hooker and Lazin 2000), so only a brief description is given here. LoCNESS and SeaSAS use 7-channel radiometers with

TABLE 1. The average environmental conditions during PROSOPE stations organized by the sequential day of the year (SDY): chlorophyll *a* concentration (C_a), wave height (H), wind speed (W), vertical tilt of the SeaSAS instruments during data collection (φ_s), diffuse attenuation coefficient at 490 nm (K_d), solar zenith angle (θ_s), and cloud cover (CC). The SF, LN, and SS cast numbers refer to the SeaFALLS, LoCNESS, and SeaSAS systems, respectively. Bold entries indicate very good environmental conditions for optical intercomparison studies: $K(490) < 0.1$ m^{-1}, $W < 10$ m s^{-1}, $H \leq 1.0$ m s^{-1}, and predominantly clear skies (CC < 4). The station number codes correspond to Fig. 1 as follows: ''U'' for the upwelling region off Agadir, ''S'' for the short daily stations, ''M'' for the very clear waters southwest of Crete, and ''D'' for the site northwest of Corsica; the numbers represent the serial encoding of the day-to-day sampling for each station type.

Station		Cast nos.			C_a	H	W	φ_s	K_d	θ_s	CC	Sky conditions during
SDY	No.	SF	LN	SS	(mg m^{-3})	(m)	(m s^{-1})	(°)	(m^{-1})	(°)	(1/8)	sampling
252	U1	1–5			2.120	0.5	5.1		0.173	26.4	0	Clear w/haze
253	U2	6–8	1–4	1–12	3.750	0.0	2.6	2.0	0.212	28.2	7	Hazy overcast
254	U3	9–11	5–7	13–19	1.570	0.5	5.1	1.0	0.120	30.3	7	Hazy overcast
255	**U4**	12–15	8–11	20–23	0.650	0.5	8.2	1.2	0.070	27.0	0	Clear w/haze
258	**S2**	16–18	12–14	24–26	0.085	1.0	8.7	2.0	0.025	34.6	2	Clear w/haze
259	S3	19–21	15–17	27–28	0.063	0.5	5.7	1.7	0.028	38.4	4	Clear w/small clouds
260	S4	22–24	18–20	29–33	0.049	0.0	4.6	1.4	0.028	35.8	6	Clear w/clouds
262	**S6**	25–28	21–25	34–38	0.028	0.5	4.6	1.7	0.028	35.1	3	Clear w/clouds and haze
263	**M1**	30–33	26–28	39–45	0.032	0.5	2.6	0.9	0.027	33.2	1	Clear w/haze
264	**M2**	34–37	29–32	46–52	0.029	0.5	5.7	0.8	0.024	33.4	0	Clear w/haze
265	**M3**	38–40	33–35	53–56	0.039	1.0	6.2	1.8	0.026	48.3	3	Clear w/clouds and haze
266	**M4**	41–44	36–39	57–64	0.035	1.0	6.7	1.4	0.022	34.5	2	Clear w/haze
267	**M5**	45–47	40–42	65–68	0.032	0.5	6.2	1.1	0.028	35.7	1	Clear w/haze
269	**S7**	48–51	43–46	69–76	0.045	0.0	2.6	0.5	0.031	39.1	0	Clear w/haze
270	S8	52–54	47–49	77–81	0.046	0.0	2.1	1.1	0.032	47.1	4	Clear w/clouds and haze
271	S9	55–57	50–52	82–87	0.082	1.0	12.3	1.3	0.032	43.9	3	Clear w/small clouds
272	**D1**	58–60	53–67	88–109	0.112	0.0	7.2	1.2	0.044	48.1	0	Clear
273	D2	61–63	68–70	110–115	0.107	1.0	7.7	1.6	0.039	48.0	5	Clear w/clouds and haze
274	D3	64–66	71–78	116–130	0.096	0.5	3.6	2.1	0.040	49.2	4	Clear w/small clouds
275	D4	67–69	79–81		0.106	0.5	4.6		0.039	53.3	5	Clear w/clouds
276	D5	70–72	82–84	131–137	0.105	0.5	2.6	1.8	0.040	50.8	5	Thin cirrus

16-bit analog-to-digital converters, and are capable of measuring light over a 4-decade range. SeaFALLS includes 13 channels with 24-bit converters (and gain switching, which was not used during PROSOPE). These in-water instruments, equipped with buoyant fins at the tail and a weight near the nose, fall vertically through the water column as a rocket-shaped package with minimum tilts (less than 2°). Within the nose, LoCNESS has two sensors to measure the upward radiance and irradiance, $L_u(\lambda, z)$ and $E_u(\lambda, z)$, respectively, while SeaFALLS has only one sensor to measure $L_u(\lambda, z)$. Both profilers are configured with a downward irradiance, $E_d(\lambda, z)$, sensor located in the tail. They are also equipped with a conductivity–temperature probe and a miniature fluorometer to provide a basic physical and biological description of the water column (Figs. 1b and 1c).

Separate intercalibrated sensors measured the above-water total solar irradiance $E_d(\lambda, 0^+)$ for each profiler; these references were mounted on the topmost level of the ship, completely free from any shading or reflecting obstacle. The profilers, connected by a 7-mm power and telemetry cable to the data acquisition systems, were deployed from the stern of the ship. They were floated approximately 30–50 m away before being released for a (usually simultaneous) free-fall profiling sequence, thereby avoiding any perturbations from the presence of the vessel.

The SeaSAS instrument includes two identical 7-channel radiometers (with different saturation thresholds), which simultaneously measure the sky radiance reaching the surface $L_{sky}(\lambda)$ and the total radiance above the surface $L_T(\lambda)$. The $L_{sky}(\lambda)$ measurement is made by pointing the radiometer skyward at a zenith angle equal to the nadir angle of the $L_T(\lambda)$ observations (here $\theta = 40°$) and within the same azimuthal plane. An external module measured the vertical (two axis) tilts and horizontal (compass) pointing of the sensors (Fig. 1d). SeaSAS could not be accommodated on the bow of the vessel, so it was mounted on the port side above the bridge (about 16.5 m above the water), with good surface viewing conditions in the azimuthal plane (±65° abeam). Under most circumstances, the heading of the vessel during data collection was maintained in such a way that the bow or stern was approximately pointed toward the sun, to allow the radiometers to be easily pointed at least 90° away from the sun.

The above- and in-water radiometers had five (blue and green) channels in common (412, 443, 490, 510, and 555 nm with 10-nm bandwidths), and the former had two near-infrared channels (780 and 865 nm). The basic data sampling procedure consisted of collecting data from all optical devices as simultaneously as possible. Handheld radios were used to coordinate the deployments and operations, and constant communication was maintained with the bridge to ensure minimal heading deviations during the sampling intervals. The above-water sensors collected data in 3-min successive sequences, whereas the in-water profiler casts usually took 6–7 min (2–3 min for measurements during profiler de-

scent, and then 3–4 min to pull the instruments back to the surface and ready them for another deployment). During stable atmospheric conditions, two SeaSAS casts were executed for each pair of in-water casts.

The length of time needed for an in-water cast was set primarily by the time needed to reach the 1% light level. The sampling time for the above-water sensors can be set using a variety of arguments. For this study, the primary objective was to make sure the variability associated with the upper ocean (which is dominated by the 5–20-s surface wave field) is well resolved, but over a time period usually permitting stable illumination. A 3-min duration for the above-water measurements was chosen, because it provides a long enough time period to sample a significant number (10 or more) of wave-slope variations associated with modulations by oceanic swell.

a. Calibration and stability

Calibration stability over the course of a campaign is potentially an important source of variance in instrument comparisons involving individual channels (Hooker and Aiken 1998; Hooker and Maritorena 2000). For SeaWiFS field campaigns, the stability of the instruments is usually monitored with the SeaWiFS Quality Monitor, but it was not possible to use this instrument during PROSOPE. The above- and in-water instruments, however, were calibrated before and after the cruise without significant change (i.e., less than 2%).

In situ measures of instrument stability are possible by taking advantage of instrument redundancy. The likelihood that two independent sensor systems would change in exactly the same manner is assumed to be extremely unlikely, so a favorable comparison of the data from two independent instruments is a suitable demonstration of the intercalibration and stability of the sensors. For the in-water sensors, this opportunity is provided by the simultaneous deployments of the two in-water profiling systems which can be radiometrically compared at all wavelengths over the entire cruise period. Although duplicate above-water systems were not deployed, the spectral stability of the sea-viewing sensor, which was also used to measure a Spectralon plaque, can be compared to the incident solar irradiance measured with the solar reference. These stability analyses are presented below (section 6a).

b. Sampling coregistration

Simple geometric calculations show that the spectral coregistration, based on the manufacturer's specification of the SeaSAS field of view, is above the 98% level from a height of 16.5 m. The mismatch would become significant (less than 90% of mutual coverage) only if the target distance is less than 2.0 m, for example, if sampling were conducted from a very small boat. For the present experiments, it has been verified that the peaks and troughs for each channel are temporally coherent and in phase with one another, so the rejection procedure and the temporal masking are fully justified. An example time series confirming the coregistration of the channels is presented in Fig. 2.

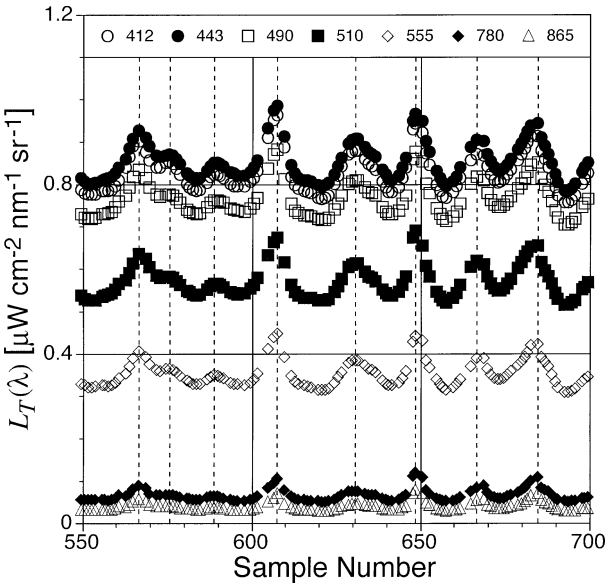

FIG. 2. A time series of $L_T(\lambda)$ data (25-s duration) from SDY 272 (clear sky, flat sea surface, and a wind speed of 7.2 m s^{-1}). The above-water sensors are pointed perpendicular to the sun plane as well as the side of the ship, $\phi = 90°$ and $\alpha_s = 0°$, respectively. The dashed lines indicate peaks in the radiance channels (identified using the 555-nm wavelength).

5. Data processing

The in-water analysis techniques are based primarily on the Smith and Baker (1984) method, hereafter referred to as S84. For above-water data analysis, several methods for surface glint correction were developed for different experimental conditions (i.e., clear or cloudy sky, Case-1 or Case-2 conditions, etc.). The two methods applicable to the PROSOPE dataset are Morel (1980) and the so-called SeaWiFS Ocean Optics Protocols (Mueller and Austin 1995; Mueller et al. 2000; hereafter, the former is referred to as M80 and the latter as S95, respectively).

a. In-water (S84) method

From the $L_u(\lambda, z)$ near-surface profiles, the attenuation coefficient $K_L(\lambda, z_0)$ is computed as the local (around the depth z_0) slope of $\ln[L_u(\lambda, z)]$. Then $K_L(\lambda, z_0)$ is used to extrapolate the upward radiance through the upper layer to determine $L_u(\lambda, 0^-)$ at null depth. The water-leaving radiance is then obtained using (3′). Because there is only one processing method, the in-water data are distinguished by the measurement sys-

tems (LN or SF as superscripts for LoCNESS and SeaFALLS, respectively).

b. Above-water (M80 and S95) methods

Above-water data processing consists of removing the contamination term, ΔL in (5), which adds to the marine signal and originates from reflections at the air–sea interface. The sky radiance reflected off the wave-roughened surface is a priori at the origin of the ΔL signal, but as shown later on, reflected radiation from the sampling platform is another source of contamination. Even if only the sky reflection is considered, its contribution to L_T is always important. For Case-1 waters in the near-infrared domain (e.g., at 780 and 865 nm), where the sea is essentially *black,* this contribution amounts to 100%, and then decreases toward shorter wavelengths where the diffuse ocean reflectance departs from zero (see discussion below with Fig. 3). In Case-2 waters, particularly when the sediment load is high, the water reflectance may deviate from zero in the near infrared and contribute to ΔL.

The M80 glint correction method is based on the existence of a black target in the near-infrared region. For all of the PROSOPE data, 865 nm is the reference infrared wavelength λ_r. The above-water radiance measured at λ_r is entirely due to surface reflection, and this estimate is extended over the whole spectrum by using the spectral dependence of the incident sky radiance $L_{\text{sky}}(\lambda)$ measured in the direction appropriate for reflection from the sea surface. Estimated glint is subtracted from the total signal to recover $L_W(\lambda)$, according to

$$L_W^{\text{M80}}(\lambda) = L_T(\lambda, \phi', \pi - \theta) - L_{\text{sky}}(\lambda, \phi', \theta)\left[\frac{L_T(\lambda_r, \phi', \pi - \theta)}{L_{\text{sky}}(\lambda_r, \phi', \theta)}\right]. \quad (9)$$

It is important to note the following: (a) in turbid Case-2 waters, the $L_W(\lambda_r) = 0$ assumption often fails and this method is not universally applicable [see Hooker et al. (2002a) for a case example]; (b) if other contaminating reflections play a part (such as those originating from the ship), they are captured when measuring $L_T(\lambda_r)$; and (c) these other contaminations have a spectral composition which may (and generally do) differ from that of the sky radiance used in (9), when the correction is extended throughout the visible spectrum.

The S95 method makes use of the same set of measurements, but they are used differently. The glint is removed through a constant interface reflectance factor ρ, which is applied to the spectral sky radiances according to

$$L_W^{\text{S95}}(\lambda) = L_T(\lambda, \phi', \pi - \theta) - \rho(\lambda, \theta)L_{\text{sky}}(\lambda, \phi', \theta). \quad (10)$$

The reflectance factor ρ would be the Fresnel reflectance averaged over the field of view of the detector pointed in the θ direction, Ω_{FOV}, if the interface was level. Generally, this is not the case, so ρ depends on the capillary wave slopes, and, thus, on wind speed (Austin 1974; Mobley 1999). The wavelength dependence originates from the normal dispersion of the refractive index of water, which is weak and can be neglected. It is worth

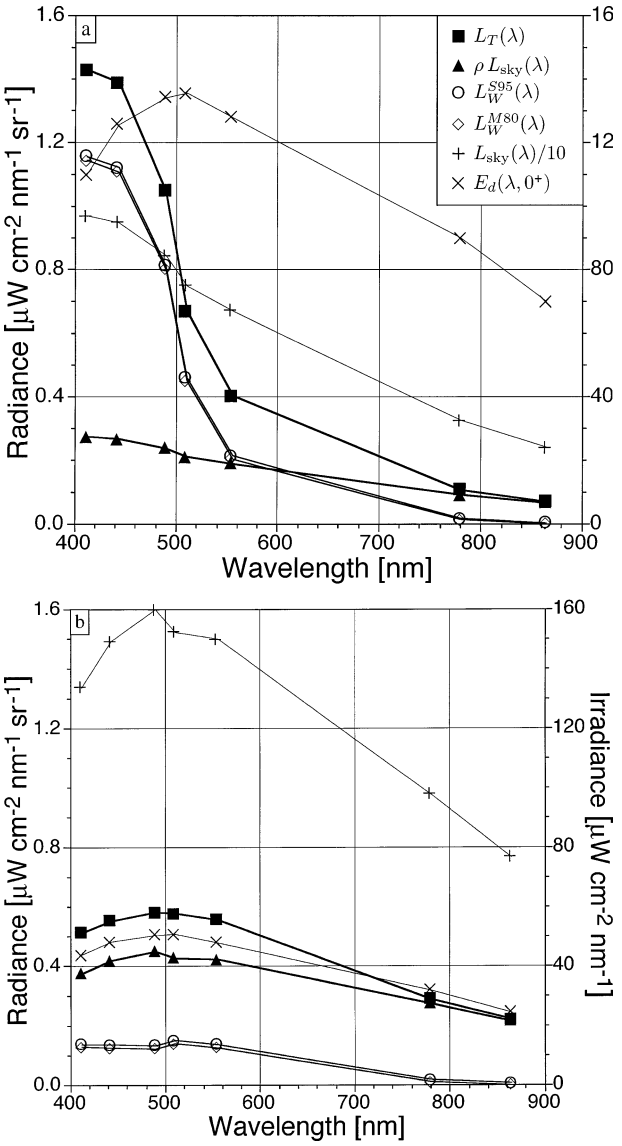

FIG. 3. Examples of spectral signals used when deriving water-leaving radiances, from the M80 and S95 methods, $L_W^{\text{M80}}(\lambda)$ and $L_W^{\text{S95}}(\lambda)$, respectively. Also shown are the downwelling irradiance $E_d(\lambda, 0^+)$ (rightmost vertical axis); the sky radiance $L_{\text{sky}}(\lambda)/10$ (scaled by a factor of 10, so the leftmost vertical radiance axis does not have to be distorted); the reflected sky radiation $\rho L_{\text{sky}}(\lambda)$; and the total surface signal $L_T(\lambda)$. Two contrasting environmental conditions are shown (using perpendicular viewing with respect to the side of the ship): (a) measurements performed in very oligotrophic water from the eastern-most part of the cruise track (SDY 264, C_a = 0.029 mg m^{-3}, and perfectly cloud-free conditions) and (b) measurements from the upwelling zone off Agadir (SDY 253, C_a = 3.75 mg m^{-3}, and hazy overcast conditions).

noting an extra source of reflected light (e.g., from the ship) is, by definition, assumed negligible when using the S95 method.

The original specifications for S95 recommended a pointing angle $\theta = 20°$ from nadir (Mueller and Austin 1995). Radiative transfer simulations above a wave-roughened surface from Mobley (1999) showed a superior angle was 40°, and that a preferred azimuth angle was 135°. With these viewing angles, the reflectance factor ρ amounts to 0.028 for $W < 5$ m s^{-1}, and increases up to about 0.04 when $W = 15$ m s^{-1}. The majority of the PROSOPE data were collected with an ambient wind close to 5 m s^{-1} (the average wind speed for the SeaSAS casts used in this study was 5.3 m s^{-1}), so the S95 results were produced using $\rho = 0.028$. A separate analysis of the data using a variable ρ produced no appreciable changes in the results (the average variable ρ value was 0.029).

Above-water signals from two contrasting situations are shown in Fig. 3; also shown are examples of the spectral $L_W(\lambda)$ values, as retrieved by applying the M80 and S95 methods. Although the $L_T(\lambda)$ and $\rho L_{\text{sky}}(\lambda)$ values converge at 865 nm in these instances, this is not always the case, as discussed later on.

Another important point is the variable contribution of $\rho L_{\text{sky}}(\lambda)$ to $L_T(\lambda)$. In Fig. 3a, dealing with clear sky and blue oligotrophic water, the sky contribution in the visible part of the spectrum is maximal (about 40%) at 555 nm, and then decreases (about 20%) for blue (412–443 nm) radiation. In contrast, Fig. 3b corresponds to a situation with hazy overcast (but bright) sky and low reflecting chlorophyll-rich waters, and $\rho L_{\text{sky}}(\lambda)$ represents about 75% of the total signal in the whole visible part of the spectrum. Note also that the incident solar irradiance peaks around 490 nm, so contamination from solar reflections (which can occur off the ship's superstructure, as discussed below) spectrally differs from reflected sky radiation, at least when the sky is not hazy and *whitish.*

c. Method revisions

All of the above-water data were collected using commonsense procedures. In particular, foam and floating material were avoided, and no data collection was initiated unless the solar disc was unobscured by clouds (and expected to remain so for several minutes) and the sky was also cloud free within a wide solid angle around the pointing angle of the sky sensor. For some days, respecting these constraints required a considerable amount of time.

Because this study is concerned with artificial perturbations from the sampling platform that affect the natural radiation field of the upper ocean, it is appropriate to consider the primary difference between how the above- and in-water methods sample the upper ocean. The effective surface area associated with an in-water estimate of $L_W(\lambda)$, derived from a vertical profile of $L_u(z, \lambda)$, is many times larger than the surface spot viewed by the above-water sensor. Surface wave effects are, therefore, effectively averaged within the in-water data, but are expressed primarily as discrete events in the above-water data. This is one possible source of a methodological bias between the two approaches, and it places a special burden on the above-water data collection and processing; that is, the sampling time must adequately capture surface variability effects, so they can be properly dealt with during data processing.

In reference to (5), the L_T signal actually results from the superposition of three contributions: (a) the steady water-leaving radiance L_W; (b) the sky glint, and possibly other reflections, ΔL, usually slowly varying with the period of the waves and swell; and (c) the mostly random, sharp, sun glint outliers produced by capillary waves. Note that even when the radiometer is pointed at least 90° away from the vertical solar plane, bright flashes from the latter occur (Fig. 2), but this third term is not identified in (5) because the sun glint spikes are removed from the high frequency spectra with the use of an appropriate filtering technique. The periodic variations of the sky glint are removed from the low frequency spectra.

Only the S95 method included a glint filter as part of the protocol. This filter, plus eight others, were evaluated by Hooker et al. (2002a) They concluded the most effective filter consisted of selecting the lowest 5% of the data in terms of radiance in the near-infrared bands, and then to use this selection as a temporal mask for all data at other wavelengths. This very high rejection rate (95% of the data recorded during each cast) was adopted for the processing of all PROSOPE data. This is an admittedly restrictive protocol that is probably more severe than most of those in common use, which are often based on some averaging and less selective procedures.

d. Statistical parameters

Three sources of $L_W(\lambda)$ estimates are available, two from in-water instruments and one from above-water measurements. Although a large number of casts were collected for each instrument, only data collected simultaneously by the three instruments are used in the following analyses to minimize any source of extraneous variance. No single method is presumed more correct than the other, so an unbiased percent difference (UPD), ψ_B^A, between two methods (A and B) providing $L_W(\lambda)$ estimates is defined as

$$\psi_B^A(\lambda_i) = 200\frac{L_W^A(\lambda_i) - L_W^B(\lambda_i)}{L_W^A(\lambda_i) + L_W^B(\lambda_i)}, \tag{11}$$

for example, the UPD between the water-leaving radiances at 412 nm estimated with the M80 and S95 methods is $\psi_{\text{S95}}^{\text{M80}}(412)$.

The relative percent difference (RPD) between two data products is computed as

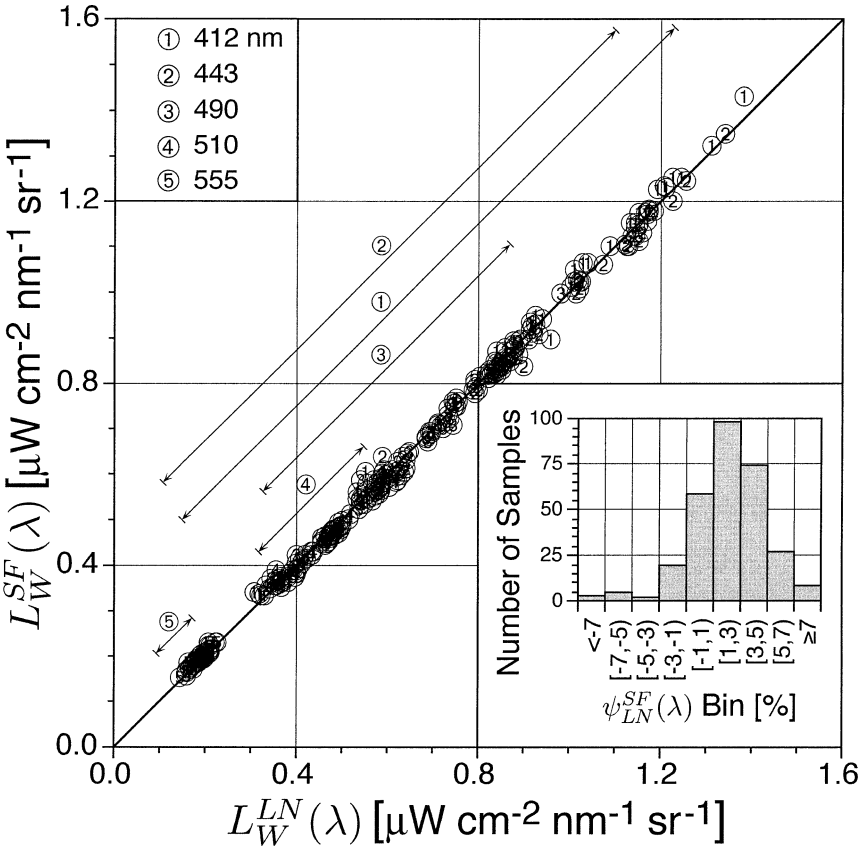

FIG. 4. The intracomparison of water-leaving radiances derived from the simultaneous deployment of the LoCNESS and SeaFALLS profilers, $L_W^{LN}(\lambda)$ and $L_W^{SF}(\lambda)$, respectively, during clear-sky conditions (59 casts). The inset panel shows the histogram of $\psi_{LN}^{SF}(\lambda)$ values. The thin diagonal lines show the radiometric extent of the water-leaving radiances for the five blue and green wavelengths.

$$\delta_B^A(\lambda_i) = 100\frac{L_W^A(\lambda_i) - L_W^B(\lambda_i)}{L_W^B(\lambda_i)}. \quad (12)$$

For the RPD computations, the *B* method must be an appropriate reference value, and in this study, it is usually an in-water measurement.

Average percent differences, formed by binning the data over a subset of *N* casts are denoted by the so-called bar accent: $\overline{\delta}_{LN}^{S95}(412)$ are the average RPD values between $L_W^{S95}(412)$ and $L_W^{LN}(412)$ for a subset of the total (simultaneous) dataset. Note that in all the percent differences, there is an implicit normalization with respect to the illumination conditions, because a ratio of radiance levels from two independent systems is always used.

6. Results

A large number of casts were collected for each sampling system (Table 1), but the desire here is to minimize any unnecessary source of variance, so the primary data used in the analyses are for when the relevant instruments were collecting above- and in-water data simultaneously. Theoretical (Gordon 1985) and empirical (Weir et al. 1994) studies of ship perturbations to the in-water light field are relevant, but do not specifically address the possible effects on above-water measurements. This study is primarily focused on the latter.

a. Above- and in-water intracomparisons

The agreement between the in-water profilers during clear-sky conditions is presented in Fig. 4. The L_w values, regardless of wavelength, are well distributed with respect to the 1:1 line, and the histogram (inset panel) shows there is approximately a 2% bias between the two datasets. This agreement is very close to the sensor calibration uncertainty, estimated to be 1.5%–2.0% (Hooker et al. 2002b). Despite the absence of independent monitoring, it can be concluded that the performances of both sensor systems were very stable during the entire cruise period. Given this excellent level of agreement, and the fact that the majority of the in-water sampling during clear-sky conditions was with the LoCNESS profiler, the $L_W^{LN}(\lambda)$ values are hereafter considered as reference, or *sea-truth*, values.

During clear-sky conditions on seven different occasions spanning six days, the sea-viewing (L_T) sensor was used to measure a calibrated gray Spectralon plaque. The irradiance values calculated for the plaque, $E_p(\lambda)$, can be intracompared to the incident solar irradiance measured with the solar reference, $E_d(0^+, \lambda)$. Although the magnitudes of the two measures are expected to be biased (gray plaques have higher calibration uncertainties from the added doping material, and the near proximity of the sea-viewing sensor *loads* the plaque with reflections), the spectral shape of the plaque irradiance should agree well with the solar reference. The intracomparison is made by normalizing all wavelengths by the value at 510 nm (the nominal peak in solar illumination). The uncertainty (and standard deviation), calculated using the RPD formulation $100[E_p(\lambda) - E_d(0^+, \lambda)]/E_d(0^+, \lambda)$, is estimated to be 2.4% (2.0%) for the spectral range 412–555 nm.

b. Glint correction comparisons

As a consequence of the principles involved in their formulations, a comparison of the output of the M80 and S95 correction methods allows the detection of any ship contamination in the L_T signal. This is because the M80 method is sensitive to, and thus, is able to identify, a ship perturbation, whereas the S95 method, based on a theoretical value of the reflectance factor, will just ignore it. The presence of a ship perturbation can be detected with the ratio

$$r(865) = \frac{L_T(865)/L_{\text{sky}}(865)}{\rho}, \tag{13}$$

where the numerator comes from M80 in (9) and the denominator from S95 in (10). Under normal circumstances, that is, in the absence of a ship perturbation, $r(865) = 1$, within the accepted variance (and provided that ρ is given a correct value). Any other reflected radiation added to the sky-reflected radiation will lead to $r(865) > 1$, and the departure from unity is an estimate of this effect.

In Fig. 5, the $r(865)$ values are plotted as a function of α_s, that is, the pointing angle of the above-water sensors with respect to the perpendicular to the ship's centerline. Although the total SeaSAS dataset is composed of 137 casts (Table 1), 9 were excluded because of sampling problems (e.g., unanticipated cloud interference, ship movement during the cast, etc.). The remaining 128 casts provide a good distribution of data with respect to α_s, and show that when the instrument is pointed perpendicular to the side of the ship ($\alpha_s = 0$), the $r(865)$ values are a little larger than 1, which suggests a reduced contamination by the ship. As the radiometers are pointed more and more toward the bow or stern, that is when the distance from the ship to the surface spot decreases, $r(865)$ dramatically increases, reaching values as high as 4–5 when $\alpha_s \approx \pm 60°$. These large ratios indicate the radiation reflected by the surface

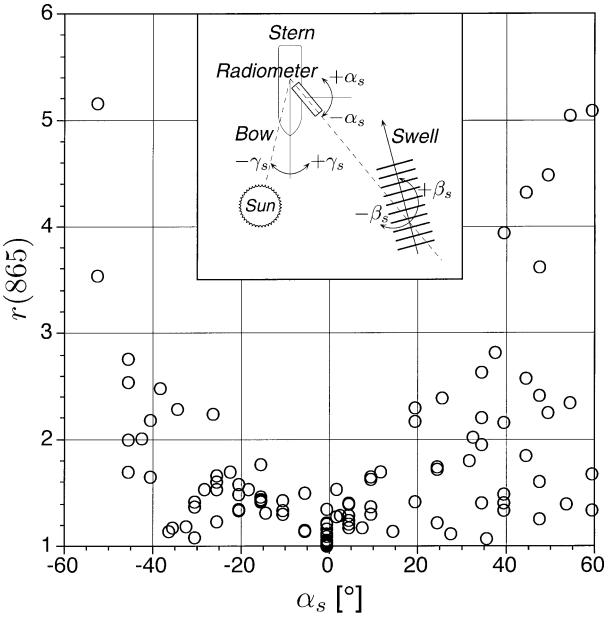

FIG. 5. The distribution of $r(865)$ as a function of α_s (negative α_s values are toward the bow and positive α_s values toward the stern). The total dataset is composed of 128 casts: 19 were in overcast conditions and 109 were in clear-sky conditions. Overcast data are not shown as separate symbols, because they fall within a narrow range (slightly larger than 1) and all at $\alpha_s = 0$, so they would obscure the clear-sky results. The inset panel shows the pointing angle of the above-water radiometers with respect to the side of the ship (α_s) as well as the ambient swell (β_s), and the angle of the sun with respect to the bow (γ_s).

and seen by the sensor is largely dominated by that originating from the superstructure.

These high values, however, are not observed in a systematic manner. For example, when $\alpha_s = 40°$ or 60°, $r(865)$ values span the interval 1–5, which deserves another kind of analysis involving γ_s, that is, the angle between the centerline of the ship and the position of the sun (Fig. 5, inset panel). According to the sign of γ_s, the port side of the ship (where the above-water radiometers were installed) is, or is not, illuminated by the sun, which makes a difference in the intensity (and spectral composition) of the light reflected from the superstructure. In Fig. 6, the $r(865)$ values shown in Fig. 5 are plotted as a function of γ_s, and five categories of data in terms of binned $|\alpha_s|$ values are identified.

The first important observation from the Fig. 6 data is that $r(865)$ is close to 1 under overcast conditions, whatever the sun orientation. Under a clear sky, $r(865)$ remains close to 1, when the sun is to starboard and the superstructure from which SeaSAS was operated is in shadow ($-120° > \gamma_s > -180°$). The converse holds true when the sun is to port ($120° < \gamma_s < 180°$), and the side of the ship where SeaSAS was measuring is directly illuminated. When γ_s is small, and the sun is almost aligned with the bow, the $r(865)$ values vary widely.

In conclusion, the contamination by the ship is re-

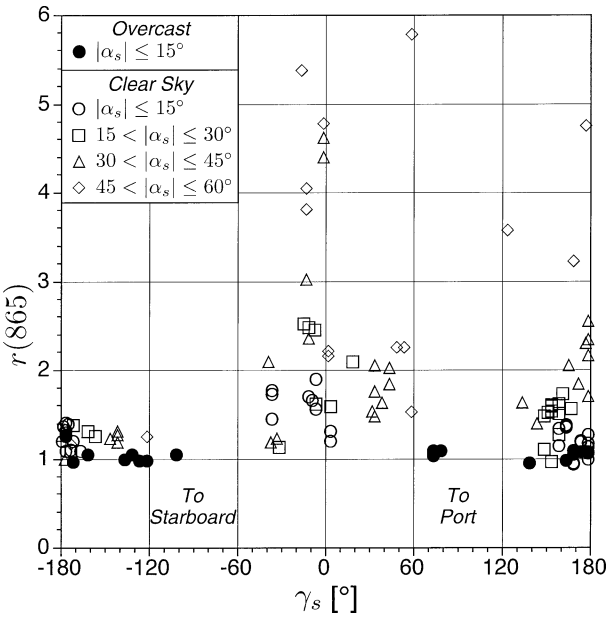

FIG. 6. The distribution of $r(865)$ as a function of γ_s (negative γ_s values are toward starboard and positive γ_s values toward port as shown in Fig. 5). The total dataset is the same as in Fig. 5, except overcast data are shown as the solid symbols, and the clear-sky data as open symbols. All the data are binned as a function of $|\alpha_s|$ (in 15° bins).

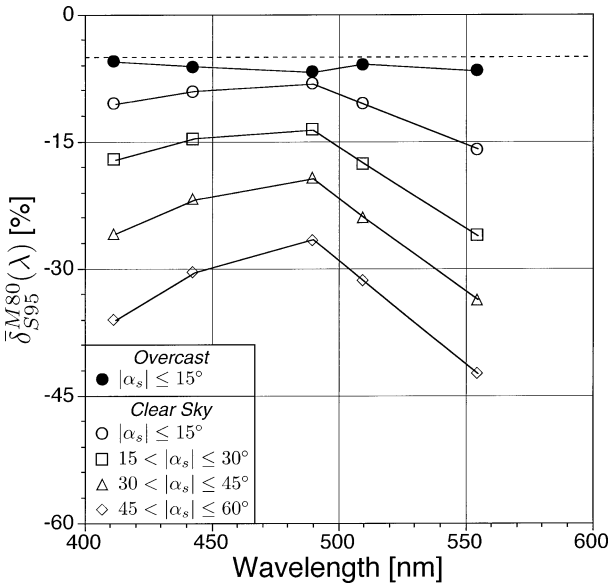

FIG. 7. The distribution of the average RPD values between the M80 and S95 methods, denoted $\bar{\delta}^{M80}_{S95}(\lambda)$. The results are split into clear-sky (open symbols) and overcast (solid symbols) conditions, and derived from 81 casts for the former and 19 casts for the latter. The dashed line represents an average underestimation of M80 with respect to S95 of −5%.

duced when the side from which the sensor is operated is in shadow, so that the superstructure is only illuminated by the sky radiation (or by uniform clouds); the contamination increases when the port side is sunlit, or if the bridge is sunlit (when γ_s is small). The geometrical aspect of the contamination is not surprising; more surprising is the importance of the effect and its complexity related to the superstructure shape. As with many ships, elements of the forward superstructure on *Thalassa* sloped to the sides of the vessel which provided reflection opportunities under a variety of sun geometries with respect to the bow.

From these results, it is possible to understand the limitations in intracomparisons between the S95 and M80 methods, because each is affected differently by the superstructure perturbation. At this point, (5) needs to be expanded (omitting the angular dependencies) as

$$L_T(\lambda) = L_W(\lambda) + \rho L_{\text{sky}}(\lambda) + \Delta L_{\text{ship}}(\lambda), \qquad (14)$$

where ρ applies to the sky radiance, $L_{\text{sky}}(\lambda)$; and $\Delta L_{\text{ship}}(\lambda)$ describes the radiance originating (i.e., reflected) from the ship's superstructure onto the water, and then reflected back into the sensor's field of view. In the S95 method, only $\rho L_{\text{sky}}(\lambda)$ is subtracted from $L_T(\lambda)$, so this method produces an overestimate of the true $L_W(\lambda)$, because $\Delta L_{\text{ship}}(\lambda)$ remains unquantified. With the M80 method, this term is known, but only at 865 nm; it is then propagated toward shorter wavelengths, using the spectral dependence of L_{sky}. To the extent that the blue sky is bluer than the direct sunlight reflected by the superstructure (particularly if painted white), the spectral extrapolation is incorrect, which leads to an overestimate of $\Delta L_{\text{ship}}(\lambda)$, and thus, to an underestimate of $L_W(\lambda)$ at short wavelengths.

Figure 7 is a plot of the average relative spectral differences between the M80 and S95 methods, during clear-sky and overcast conditions, and presented in a variety of $|\alpha_s|$ bins. Several aspects are worth noting.

1) As expected (Fig. 3), the M80 $L_W(\lambda)$ values are persistently less than those derived from the S95 method.
2) The overcast data show a minimal and spectrally constant difference, because $\Delta L_{\text{ship}}(\lambda)$ is minimal, and its spectral composition and that of L_{sky} are similar. In these specific circumstances, the M80 results are the most accurate; by neglecting the ΔL_{ship} term, the S95 results are systematically overestimated by about 5%.
3) For the clear-sky data, the difference between the two methods is noticeable, even when $|\alpha_s| < 15°$, and increases when α_s and, thus, $\Delta L_{\text{ship}}(\lambda)$ increases; these differences exhibit a spectral shape, which will be discussed later (section 6d).

c. *Above- and in-water intercomparisons*

The in-water data are free from the perturbations caused by the ship's superstructure, and can be used to determine their magnitude. The intercomparison is made with a reduced dataset composed of 49 casts (at 5 wavelengths), because (a) the two types of measurements

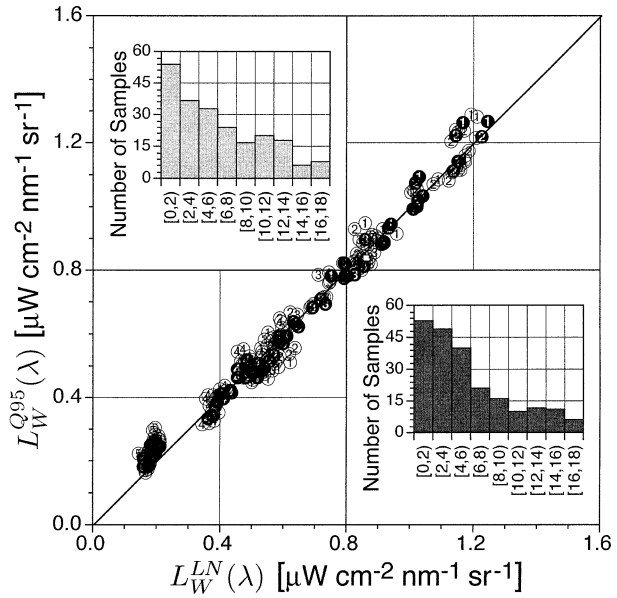

FIG. 8. The intercomparison of above- and in-water estimates of $L_W(\lambda)$ during clear-sky conditions. The former are derived from the LoCNESS data, $L_W^{LN}(\lambda)$, and the latter using SeaSAS data with the S95 method plus the bidirectional (Q-factor) correction $L_W^{Q95}(\lambda)$. The inset panels show the histograms of the absolute RPD values between the above- and in-water methods for uncorrected versus corrected data, $|\delta_{LN}^{S95}(\lambda)|$ (upper-left light bars) and $|\delta_{LN}^{Q95}(\lambda)|$ (lower-right dark bars), respectively. The total dataset is composed of 49 simultaneous casts which are separated into two groups (14 and 35 casts, respectively): $|\alpha_s| \leq 15°$ (solid circles), and $|\alpha_s| > 15°$ (open circles); the numerals within the symbols follow the wavelength convention of Fig. 4.

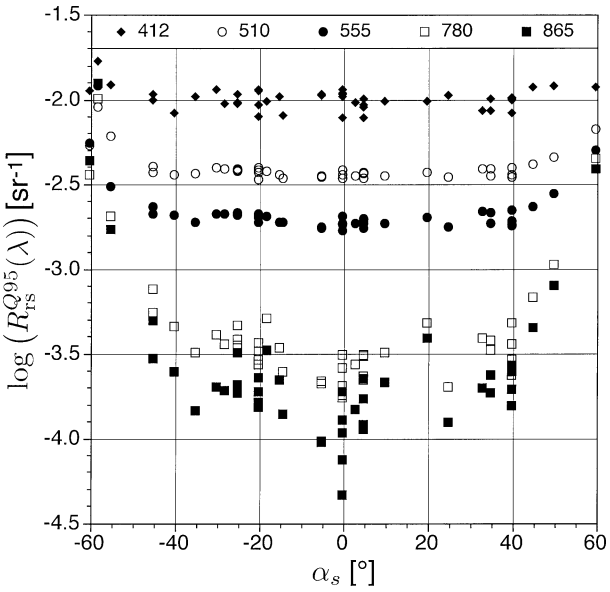

FIG. 9. The distribution of $R_{rs}^{Q95}(\lambda)$ as a function of α_s for the quasi-simultaneous casts (i.e., the above- and in-water casts were taken on average to within 3 min of each other, but occasionally as much as 10 min) for SDY 260–270 during clear-sky conditions, low wind speed (close to, or less than, 5 m s^{-1}, which means ρ is nearly constant), and low chlorophyll a concentrations ($C_a < 0.05$ mg m^{-3}). The reflectances in the visible part of the spectrum are corrected for the bidirectional effects; those in the near IR are unchanged. Only five wavelengths are shown for clarity (the 443- and 490-nm data fall in between the 412- and 510-nm data).

(above- and in-water) do not always overlap, and only those that are exactly coincident in time are kept; (b) the above-water casts are restricted to clear-sky conditions and $90 \leq \phi \leq 135°$; and (c) the data with a pointing angle $|\alpha_s| > 45°$ are discarded, because there were only four simultaneous above- and in-water casts in this bin interval. Among the clear-sky data, only those corresponding to the most stable environmental conditions (and Mediterranean Sea waters) are considered. The intercomparison of L_W^{S95} (above-water, SeaSAS data, and the S95 method) and L_W^{LN} (in-water, LoCNESS data, and the S84 method), is made under these restrictions.

Because of bidirectional effects, the above- and in-water radiances are not straightforwardly comparable; L_W^{S95} must first be converted into a corrected water-leaving radiance using (6). Indeed, the above-water measurements, made at $\theta = 40°$ (whence $\theta' = 29°$), must be transformed on a case-by-case basis as if they were made vertically ($\theta = 0°$). The transformation uses look-up tables derived from calculations for a clear sky, as discussed in Morel and Gentili (1996), which depend on θ', λ, the chlorophyll a concentration, and ϕ, the azimuthal difference (between the viewing and solar planes).

The PROSOPE measurements were often made around midday, so the solar zenith angle (θ_s) was never very large, 33°–50° (Table 1); such values, combined with ϕ values between 90° and 135° and low chlorophyll concentrations (in the Mediterranean Sea), do not lead to a considerable bidirectional correction. The slant radiance slightly exceeds the nadir radiance by approximately 2%–4% (note that for low solar elevation, the increase is much more significant). The bidirectionally corrected data, denoted L_W^{Q95}, are shown in Fig. 8 along with the comparative histograms for the uncorrected and corrected data. The principal consequence of the Q-factor correction is a stronger central peak with fewer outliers.

Figure 8 also shows the $L_W^{Q95}(\lambda)$ values not only overestimate $L_W^{LN}(555)$, but the relative magnitudes of the overestimates tend to increase quasi-linearly with increasing radiance (in keeping with the postulated contamination from superstructure reflections at this wavelength). An inspection of the other wavelengths reveals this effect is only well expressed at the 555-nm wavelength (this is most easily seen in the solid symbols which are all well distributed around the 1:1 line across the entire range of radiance levels).

d. Spectral intercomparisons

Figure 9 is a plot of $R_{rs}^{Q95}(\lambda)$ (the remote-sensing reflectance determined from the S95 method and corrected for bidirectional effects) as a function of α_s; the remote

TABLE 2. A summary of the average RPDs and corresponding Type B uncertainties between the above- and in-water estimates of water-leaving radiance in each $|\alpha_s|$ 15° bin, $\overline{\delta}_{\mathrm{LN}}^{\mathrm{abw}}(\lambda)$, with the above-water estimates corrected for bidirectional effects: $\overline{\delta}_{\mathrm{LN}}^{Q95}(\lambda)$, in the top quarter of rows, and $\overline{\delta}_{\mathrm{LN}}^{Q80}(\lambda)$ in the second; the Type B deviations are given in the bottom two quarters, respectively. The three rightmost columns present the band-ratio results. The number of casts in each $|\alpha_s|$ bin and for the overall dataset is given by *N*.

Method and statistic	$\lvert\alpha_s\rvert$ Bin interval [°]	Casts *N*	$\overline{\delta}_{\mathrm{LN}}^{\mathrm{abw}}(\lambda)$ [%]							
			412	443	490	510	555	443/555	490/555	510/555
*Q*95 RPD	$\lvert\alpha_s\rvert \le 15°$	14	−1.8	−1.9	−4.5	−3.8	13.2	−13.0	−15.3	−14.8
	$15° < \lvert\alpha_s\rvert \le 30°$	16	−1.2	−0.8	−3.1	−1.1	18.2	−15.6	−17.6	−16.0
	$30° < \lvert\alpha_s\rvert \le 45°$	19	−2.9	−1.6	−3.5	−0.1	20.9	−17.9	−19.6	−17.0
	Overall average	*49*	*−2.0*	*−1.4*	*−3.7*	*−1.5*	*17.8*	*−15.8*	*−17.7*	*−16.0*
*Q*80 RPD	$\lvert\alpha_s\rvert \le 15°$	14	−11.1	−10.1	−12.1	−14.5	−6.7	−3.4	−5.4	−8.1
	$15° < \lvert\alpha_s\rvert \le 30°$	16	−15.6	−13.7	−15.3	−18.0	−13.0	−0.3	−2.0	−5.2
	$30° < \lvert\alpha_s\rvert \le 45°$	19	−27.0	−22.3	−21.7	−23.9	−20.4	−2.3	−0.6	−3.7
	Overall average	*49*	*−18.7*	*−16.0*	*−16.9*	*−19.3*	*−14.1*	*−1.9*	*−2.4*	*−5.4*
*Q*95 Type B dev	$\lvert\alpha_s\rvert \le 15°$	14	3.4	2.7	2.6	2.8	8.9	4.3	4.0	2.7
	$15° < \lvert\alpha_s\rvert \le 30°$	16	6.7	4.8	3.8	5.5	11.9	4.9	4.8	3.7
	$30° < \lvert\alpha_s\rvert \le 45°$	19	5.6	4.9	4.4	7.6	14.9	6.4	5.5	3.6
	Overall average	*49*	*5.2*	*4.1*	*3.6*	*5.3*	*11.9*	*5.2*	*4.8*	*3.3*
*Q*80 Type B dev	$\lvert\alpha_s\rvert \le 15°$	14	9.4	6.3	3.9	4.9	8.9	2.9	4.0	2.7
	$15° < \lvert\alpha_s\rvert \le 30°$	16	11.3	8.2	5.5	6.4	11.1	5.7	6.2	4.8
	$30° < \lvert\alpha_s\rvert \le 45°$	19	15.3	10.4	6.2	6.8	10.9	4.5	7.5	5.7
	Overall average	*49*	*12.0*	*8.3*	*5.2*	*6.0*	*10.3*	*4.4*	*5.9*	*4.4*

sensing reflectance is used to cancel out, in a simplified way, variations due to changing solar illumination. The data shown are only those for the Mediterranean Sea, with low chlorophyll *a* concentration ($C_a < 0.05$ mg m^{-3}) and clear-sky conditions. Consequently, the station-to-station differences in $R_{\mathrm{rs}}^{Q95}(\lambda)$ are rather weak, so the dependency of reflectance on α_s is not obscured by local differences, and the trends in Fig. 9 are significant. This figure shows the ship perturbation is characterized by the following:

1) a good symmetry with respect to $\alpha_s = 0$, which suggests rather homogeneous reflective properties of the superstructure, from the bow to the stern, when similarly lit;
2) as already noted, an increase in reflectance, actually in $\Delta L_{\mathrm{ship}}(\lambda)$, as a function of α_s; and
3) an increase of this perturbation as a function of λ—from weak, but detectable, levels at 412 nm, to large values (a factor of 5–10) in the infrared part of the spectrum.

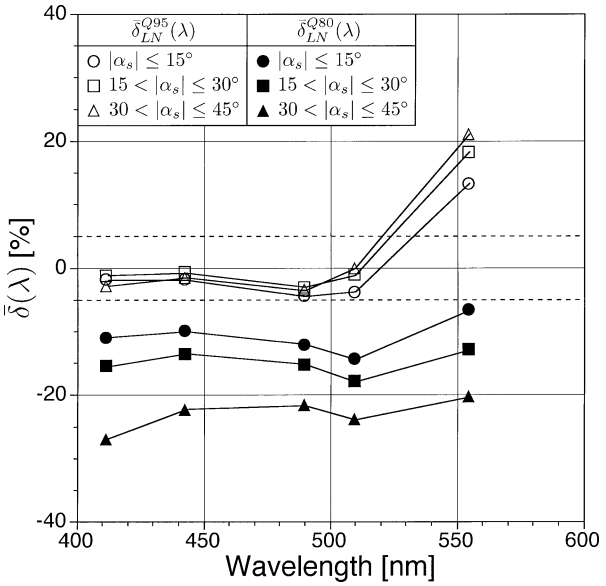

FIG. 10. A comparison of average RPDs between simultaneous in-water estimates of $L_W(\lambda)$ (from LoCNESS) and above-water estimates corrected for bidirectional effects *Q*80 (solid symbols) and *Q*95 (open symbols), as a function of $|\alpha_s|$ during clear-sky conditions (49 casts). The dashed lines indicate the ±5% difference limits.

These qualitative observations need to be considered in relation to the varying proportions of the three components of the total surface signal in (14). The relative contribution of ΔL_{ship}, maximal when L_W is negligible (in the infrared part of the spectrum), progressively decreases as L_W increases (Fig. 3a) toward the blue end of the spectrum.

Table 2 and Fig. 10 present the average RPDs between the S95 and M80 estimates of water-leaving radiances corrected for bidirectional effects and the in-water estimates, $\overline{\delta}_{\mathrm{LN}}^{Q95}(\lambda)$ and $\overline{\delta}_{\mathrm{LN}}^{Q80}(\lambda)$, respectively, as a function of the $|\alpha_s|$ pointing angle (in 15° bins). For these blue waters, and when using the S95 method, the overall difference in water-leaving radiances at a single wavelength is usually small (to within 5%), except at 555 nm (as noted in Fig. 8), where it reaches values as high as 13%, and even 21%, as a consequence of a lower marine signal at this wavelength (Fig. 4). When using the M80 method, the differences, almost spectrally neu-

tral, are always strongly negative, because of the overestimation of the $\Delta L_{\text{ship}}(\lambda)$ term (as previously noted).

Because band ratios are generally in use in ocean color algorithms (O'Reilly et al. 1998), and sometimes as simplified measurements for sensor validation, the average differences between ratios derived from above-water measurements and those derived from in-water measurements are also displayed in Table 2. The large contamination of the 555-nm channel with the S95 method results in poor agreement for the three ratios considered (much larger uncertainties that the spectral intracomparison uncertainty presented in section 6a). In contrast, the almost equal overestimates, inherent with the M80 method, cancels out when forming the band ratios, so that the corresponding average differences remain small. This apparent agreement cannot be generalized, because it depends on the spectral composition of the superstructure albedo.

The so-called Type B deviations in the RPD values within each $|\alpha_s|$ bin are presented in the bottom half of Table 2. This measure of dispersion is constructed by first computing the standard deviations with respect to the average RPD value in each bin. The standard deviations necessarily overestimate the true deviations associated with platform perturbations, because they also contain differences arising from sensor calibration, data processing, and in situ stability. A more accurate measure of the deviation caused by the presence of the ship is calculated by assuming relative standard uncertainties for the latter three effects (Hooker and Maritorena; Hooker et al. 2001, 2002a, b) which are then subtracted in quadrature from the calculated standard deviation of a particular $\overline{\delta}_{\text{LN}}^{\text{abw}}(\lambda)$ value. This difference is interpreted as a Type B relative combined deviation.

The deviations in Table 2 support several important aspects of the average RPD values. First of all, the large RPD values are well resolved, because the corresponding deviations are much smaller. Second, there is a general trend of decreasing deviations from 412–490 nm, which then increase from 510–555 nm. This trend is well summarized by the overall deviation averages, and is in agreement with the behavior seen in Fig. 7. Third, the deviations basically increase with increasing $|\alpha_s|$. Finally, the deviations in the band ratios are usually smaller.

In Case-1 waters, the M80 and S95 techniques do not usually underestimate the water-leaving radiance. As shown by Hooker et al. (2002a), the M80 and S95 techniques usually overestimate the water-leaving radiance, so the underestimation in Table 2 across all channels for the M80 method plus the 412–510-nm wavelengths for the S95 method cannot be explained by methodological biases in the above-water algorithms. Furthermore, Hooker et al. (2002a) also showed the band ratios from above-water methods in Case-1 and Case-2 waters usually agree with in-water estimates to within 5%, so the large uncertainties for the band ratios in Table 2 are not attributed to methodological biases.

e. Ship perturbation correction

The perturbation effect is detectable through the use of the $r(865)$ ratio; its departure from unity forms a sensitive diagnostic parameter in Case-1 waters. Once detected, the next step is to examine whether a correction for this perturbation is possible with the available data. A simplified correction scheme can be constructed at every wavelength using the superstructure reflection term in the infrared. This spectrally constant model is expressed as

$$\begin{aligned}\Delta L_{\text{ship}}(\lambda) &= \Delta L_{\text{ship}}(865)\\ &= L_T(865) - \rho L_{\text{sky}}(865).\end{aligned} \tag{15}$$

A spectrally dependent model can also be constructed, which has something in common with that developed for the *residual term* mentioned in Mueller (2000a,b) or in Toole et al. (2000). This scheme actually rests on the assumption of a *white* reflection by a ship's superstructure illuminated by the sun and the sky. Under this assumption, $\Delta L_{\text{ship}}(\lambda)$ will have the same spectral composition as $E_d(\lambda, 0^+)$, and is expressed as

$$\Delta L_{\text{ship}}(\lambda) = [L_T(865) - \rho L_{\text{sky}}(865)]\frac{E_d(\lambda, 0^+)}{E_d(865, 0^+)}. \tag{16}$$

The results of using these two correction schemes are presented in Table 3 (and are to be compared with the $Q95$ results presented in Table 2). Whatever the scheme, the corrections result in lower $L_W^{\text{LN}}(\lambda)$ values, by a few percent for the 412–510-nm wavelengths, and more considerably at 555 nm, where the uncorrected values are significantly high (Fig. 10). The spectrally dependent model is more efficient than the neutral model in correcting the 555-nm channel; the corrected value (at 555 nm) still remains above the in-water value.

Admittedly, the ship perturbation correction hypotheses underlying (15) and (16) are questionable, although the latter could be more realistic, if the superstructure paint was close to that of a neutral reflector. In summary, the results of the corrections are in the right direction, without being fully satisfactory. To the extent that the 555-nm channel has not been fully corrected, the band ratios computed from the L_W^{abw} measurements remain inaccurate.

f. Clouds and oceanic swell

Among various environmental conditions, cloudiness has been identified as having a potential effect on the above-water determination of water-leaving radiances. If the excellent conditions in terms of cloud cover (CC in octa) with respect to the threshold $\text{CC} < 3$ are compared to the remaining data, no systematic effect related to varying cloudiness can be detected (apart from those described for hazy overcast conditions) and the $\delta_{\text{LN}}^{\text{S95}}(\lambda)$ and $\delta_{\text{LN}}^{\text{M80}}(\lambda)$ values are mostly unchanged. It must be emphasized, however, that the measurements were only

TABLE 3. A summary of $\overline{\delta}_{LN}(\lambda)$, values for the spectrally constant (top half) and spectrally dependent (bottom half) ship perturbation correction schemes as a function of the $|\alpha_s|$ pointing angle (in 15° bins). The number of casts in each $|\alpha_s|$ bin and for the overall dataset is given by *N*.

Correction method	$\lvert\alpha\rvert$ Bin interval [°]	Casts *N*	$\overline{\delta}_{LN}(\lambda)$ [%] 412	443	490	510	555	443/555	490/555	510/555
Constant	$\lvert\alpha_s\rvert \le 15°$	14	−0.4	−0.6	−3.7	−4.6	9.5	−9.1	−11.9	−12.7
	$15° < \lvert\alpha_s\rvert \le 30°$	16	0.5	1.0	−1.9	−1.7	13.8	−11.0	−13.5	−13.3
	$30° < \lvert\alpha_s\rvert \le 45°$	19	−0.9	0.6	−1.9	−0.3	16.5	−13.3	−15.4	−14.2
	Overall average	*49*	*−0.3*	*0.4*	*−2.4*	*−2.0*	*13.6*	*−11.3*	*−13.8*	*−13.5*
Dependent	$\lvert\alpha_s\rvert \le 15°$	14	−1.0	−1.4	−4.9	−6.5	5.6	−6.5	−9.8	−11.4
	$15° < \lvert\alpha_s\rvert \le 30°$	16	−0.4	−0.3	−3.7	−4.5	8.0	−7.5	−10.6	−11.4
	$30° < \lvert\alpha_s\rvert \le 45°$	19	−1.9	−0.9	−4.0	−3.7	9.8	−9.5	−12.2	−12.1
	Overall average	*49*	*−1.2*	*−0.8*	*−4.1*	*−4.8*	*8.0*	*−8.0*	*−11.0*	*−11.6*

made if a large fraction of the sky (around the viewing angle of the SeaSAS sky sensor) was cloud free, even when CC > 3.

One common feature of the oceanic environment, unaddressed in the protocols for above-water measurements, is how to point the surface-viewing radiometer with respect to the ambient wave field. The possible importance of swell on deriving $L_W^{abw}(\lambda)$ was partially quantified by Hooker et al. (2002a), who showed two above-water systems pointed opposite to one another with respect to the surface wave field, but still in keeping with the pointing requirements with respect to the sun, can differ (on average) by an additional 3%–7% (during clear-sky conditions).

The effects of surface gravity waves on the above-water measurements can be addressed by splitting the 49 simultaneous above- and in-water casts into two groups: (a) calm casts with no discernible swell (and thus, no swell direction), and (b) casts with a clear swell presence and direction. This produces balanced datasets with 22 casts for calm conditions and 27 for swell. Values of $\overline{\delta}_{LN}^{S95}(\lambda)$ were calculated for each group (and each $|\alpha_s|$ bin), and then the calm values were subtracted from the swell values to produce a net percent difference (NPD). The important conclusions regarding the NPD results as a function of $|\alpha_s|$ (top half of Table 4) are (a) the majority of the individual wavelengths have negative net difference values, which means the presence of swell results in lower above-water estimates of $L_W(\lambda)$; and (b) the depressive effect of swell is more accentuated at the 412-nm wavelength (independent of α_s) and is almost insignificant at the other wavelengths.

Another aspect of the surface gravity wave field can be considered in relation to the angle β_s, that is, the angle between the radiometer and the swell direction (Fig. 5, inset panel). If the radiometer is pointed in the same direction the swell is moving toward, $\beta_s = 0°$; if pointed in the opposite direction, $\beta_s = \pm 180°$. The data can be binned as a function of β_s to categorize the data in terms of the wave field (45° bins are used here): the sensor is viewing (a) the wave crests moving away, $|\beta_s| \le 45°$; (b) along the wave troughs, $45 < |\beta_s| \le 135°$; and (c) the oncoming wave crests, $135 < |\beta_s| \le 180°$. Again, the calm data are subtracted from the swell data, and the results (bottom half of Table 4) are as follows.

1) Measurements along the wave troughs are a significant local minimum, which means they are radiometrically darker than the wave crests at all wavelengths;

TABLE 4. A summary of $\overline{\delta}_{LN}^{S95}(\lambda)$, values for the NPD analysis as a function of the $|\alpha_s|$ pointing angle (in 15° bins) and the $|\beta_s|$ swell angle (in 45° bins). The number of casts in calm conditions is given by N_c, and the number of casts in the presence of swell by N_s (the N_c and N_s values in the *Overall average* rows are totals). Note that the majority of the swell data is for the above-water radiometer pointing down the wave troughs ($45° < |\beta_s| \le 135°$), which is a consequence of the ship being preferentially pointed into the swell during station work.

Calculation method	Bin interval [°]	Casts N_s	N_c	Swell − calm $\overline{\delta}_{LN}^{S95}(\lambda)$ values [%] 412	443	490	510	555	443/555	490/555	510/555
NPD	$\lvert\alpha_s\rvert \le 15°$	9	5	−4.0	−2.4	−1.3	−1.0	−1.0	−2.0	−0.8	−0.3
	$15° < \lvert\alpha_s\rvert \le 30°$	7	9	−4.2	−2.0	−0.6	−0.1	0.0	−1.6	−0.6	−0.3
	$30° < \lvert\alpha_s\rvert \le 45°$	11	8	−4.3	−0.8	0.6	0.4	−2.4	−0.6	1.1	1.5
	Overall average	*27*	*22*	*−4.1*	*−1.7*	*−0.4*	*−0.2*	*−1.2*	*−1.4*	*−0.1*	*0.3*
NPD	$\lvert\beta_s\rvert \le 45°$	4		−2.3	−2.8	−2.7	0.6	5.3	−5.7	−4.9	−3.7
	$45° < \lvert\beta_s\rvert \le 135°$	16		−5.3	−3.8	−3.4	−2.4	−6.1	1.8	2.7	2.1
	$135° < \lvert\beta_s\rvert \le 180°$	7		−3.4	−1.6	−0.5	3.0	4.5	−3.4	−1.6	−0.5
	Overall average	*27*	*22*	*−3.7*	*−2.8*	*−2.2*	*0.4*	*1.2*	*−2.5*	*−1.3*	*−0.7*

2) the darkening effect is the largest at 412 and 555 nm; and
3) at 510–555 nm, a converse trend (i.e., a brightening) seems to occur.

Note, the band-ratio data are also diversely affected by the presence of swell.

As noted before, the relative ship perturbation is the largest at 555 nm. Inasmuch as the magnitude of ΔL_{ship} interacts with the wave orientation, it is not surprising that the response of this channel is more affected (enhanced or depressed) by the swell orientation. It must be remembered, however, that the glint filter has, in principle, removed any signals artificially brightened by wave passage, because only the darkest 5% of the data are used for deriving $L_W^{\text{abw}}(\lambda)$. In summary, the swell effects are significant, spectrally dependent, and varying with the sampling geometry. The brightening–darkening alternation is related to the position of focal areas beneath the wave crest and to the horizontal inhomogeneity of the downward radiance field in the presence of waves (Zaneveld et al. 2001). The question is still open, and dedicated experiments are definitely needed to understand and properly account for these effects (which are not considered in the present above-water protocols).

7. Conclusions

Although in-water measurements have successfully been used for deriving water-leaving radiances and validating ocean color sensors, above-water measurements form an alternative, which remain to be comparatively evaluated. This was the first objective of this study, while the second one was to quantify the perturbations due to the sampling platform and environmental conditions on the above-water measurements.

Two independent, but intercalibrated, profiling instrument systems provided the same results (within 2%) in terms of $L_w(\lambda)$, and satisfied the radiometric requirements under all conditions. The measurements were carried out in clear Case-1 waters under mostly cloud-free skies, so the extrapolation procedures were accurate and not degraded by instrument self-shading uncertainties. These $L_w(\lambda)$ values can safely be (and were) used as reference values, to which the results of the above-water determinations, once corrected for the bidirectional dependency, were compared. This approach permitted the biases possibly affecting the latter to be discerned.

To the extent that sun glint does not contaminate the above-water data, accomplished here using a high rejection rate (95%) of the brightest recorded data, removing the skylight reflection, or other kinds of reflections, is the major problem when processing the above-water measurements. In spite of very good conditions in general, considerable effort, and a large number of sampling opportunities, the desired agreement between the above-water $L_w(\lambda)$ values and the in-water reference values (within $\pm 5\%$) was only achieved approximately half the time, and only for the $Q95$ method. Unfortunately, the band-ratio results for the latter were significantly degraded by the ship perturbation effect and were rendered useless for most bio-optical applications.

Considering the flaws already identified when using above-water methods (O'Reilly et al. 1998; Fougnie et al. 1999), this rather low rate of success is not surprising, albeit somewhat discouraging, particularly when considering that more adverse (sea and sky) conditions are common. In rough sea states (without foam, however), the swell and its orientation are another source of inaccuracies not yet understood.

With *Thalassa*, the ship shadow and the hull albedo effects were significantly smaller than, and appeared mostly inseparable from, the perturbation related to the superstructure albedo. The main source of discrepancy between the above- and in-water determinations of water-leaving radiances originates from the additional reflection by the ship's superstructure, which is generally poorly quantified, if not simply ignored. The use of two methods (S95 and M80) when processing the above-water data allowed the presence of this perturbation to be detected using a *diagnostic parameter*, the $r(865)$ ratio, and its departure from unity established the degree of contamination.

This ratio was found to be close to unity in only a few occurrences (Figs. 5 and 6), which means superstructure contamination was the general rule in the present above-water measurements, and was considerable in some instances. Deriving this diagnostic parameter is an easy way to detect the presence of such contaminations (as well as any other unexpected contamination by any source brighter than the water itself), and this method can be recommended in Case-1 waters (and likely in dark Case-2 waters dominated by yellow substance). Indeed, in Case-1 waters $L_w(865)$ is about two orders of magnitude below the water-leaving radiances within the visible part of the spectrum (Fig. 3; Siegel et al. 2000), thus the quantity $L_T(865)$ can safely be considered as exempt from any marine signal (not true in Case-2 waters dominated by sediment).

Another perturbation possibly influencing the $r(865)$ value deserves examination. The portion of the sky sampled by a wave-roughened sea surface dramatically widens with increasing wind speed (Mobley 1999; Toole et al. 2000). This widening, however, does not affect the $r(865)$ parameter if the portion of the sky remains homogeneous (i.e., does not contain bright clouds not seen by the narrow angle sensor used to measure L_{sky}). To ensure the robustness of $r(865)$ as a diagnostic parameter, this experimental constraint must be respected. The choice of a correct value for ρ accounting for the actual wind speed (Mobley 1999) is also a requirement to preserve the significance of $r(865)$.

Avoiding this ship contamination cannot be achieved through the use of polarizing systems, because its angular origin differs from that of the reflected sky radiation (and of the Brewster incidence angle). Correcting

for this identified contamination is, in practice, questionable; attempts to do so proved to be rather inoperative (Table 3), within the limits of a 5% radiometric accuracy objective. To develop a more efficient correction scheme, the spectral signature of the ship under various illumination conditions is needed, which is practically an unsurmountable task.

If it is easily realized that the contamination affects the $L_W^{abw}(\lambda)$ retrievals, a natural reaction is to believe band ratios are much less degraded. In other words, a sensor validation, or a vicarious calibration, based only on color ratios would be more accurate and more readily achieved. Unexpectedly, the present results have demonstrated the opposite. Although accurate $L_W^{abw}(\lambda)$ values (via the S95 method) were occasionally obtained at three wavelengths (412, 443, and 490 nm), the band ratios remained severely affected, because of the failure in properly correcting the 555-nm channel (at least in blue waters), because of the relatively low signal at this wavelength. For the same reason, correcting low signals typical of dark (yellow substance dominated) Case-2 waters is likely problematic.

Regarding the effect of surface gravity waves on the radiation field and their interaction with the superstructure reflections, a satisfactory explanation for this effect remains to be found, and specific studies under more controlled circumstances are needed.

From the behavior of the ship influence with increasing distance between the ship and the surface spot seen by the sensor, it can be approximately inferred by extrapolation that the perturbation from *Thalassa* would have been avoided if the horizontal distance was about 18 m. For a pointing perpendicular to the side of the ship, and $\theta = 40°$, this would have required a sensor operated 21 m above the water. Beside the fact that this was not possible aboard *Thalassa,* such a mounting is not optimal, as the higher the instrument is mounted, the more it is negatively influenced by ship motion. Often, the largest opportunities for making choices about competing viewing requirements (sun, swell, and ship influence) come from sensors mounted or operated from the bow, at least when the vessel is not underway. The choice of the bow is not always possible (nor practical, because of pitching), and some ships have the largest part of their superstructures close to the bow. In any case, each vessel is a particular case, and each day at sea with its specific wave orientation, cloudiness, ship heading, and sun position is a separate challenge.

These remarks emphasize the difficulties of above-water measurements, which are finally more difficult and demanding, and even more time consuming, than in-water measurements. Such measurements are perhaps inevitable in Case-2 waters, and also in Case-1 waters when performed from a ship of opportunity sailing without stopping. The possibility of getting reliable data with an acceptable yield from above-water measurements in various conditions remains unproven. Consider, for example, a scenario wherein an above-water system is mounted on a cargo vessel, or a ferry. Whether positioned in a fixed orientation, or handheld and operated by a sailor or even a scientist, safe and convenient access to the sensors usually requires the equipment to be positioned at a location that is not the highest point on the ship. If the system is fixed and autonomous, the data will be taken under largely unknown environmental conditions, and unfavorable geometries. If it is manually operated, within a limited amount of time and in the absence of corroborating information from other instruments, the problem remains about the same. It seems rather unlikely, therefore, that data with radiometric uncertainties below 5%, as required for meaningful calibration and validation activities, can be obtained using this approach. Precise metrology, dedicated and sufficient ship time, and maybe improved (gimbaled) instrumentation are needed to reach an accuracy commensurate with the requirements of vicarious calibation and algorithm validation.

A unique above-water measurement protocol is not yet defined and validated (Mueller et al. 2000), but several recommendations can be derived from the results presented here.

1) A high observation location is needed to maximize the distance between the ship and the area of the sea viewed by the sea sensor.
2) The sea-viewing sensor should be pointed toward a spot on the sea which contains the smallest solid angle of the ship with respect to the sun (i.e., an approximate cone can be constructed from the sun to the farthest extents of the ship, and the field of view of the radiometer should be positioned to minimize any intersection with this cone).
3) The portion of the sky that must be cloud free has to be much larger than the field of view of the sky sensor.
4) A nadir pointing angle equal to 50° should be considered, which is still acceptable according to Mobley (1999), because it allows the horizontal distance between the ship and the area sampled on the sea to be increased.
5) If the water type is appropriate (Case-1 waters and possibly Case-2 waters dominated by yellow substance), the $r(865)$ parameter should be used to detect platform contamination in the sea-viewing sensor data.
6) Finally, the wave height plus the geometrical relationship between the sea-viewing sensor and the swell direction should be noted (for further interpretation).

Acknowledgments. The PROSOPE optical dataset could not have been collected at the high level that was achieved without the unselfish contributions of H. Claustre and M. Babin (Université Pierre et Marie Curie). All of the optical data were acquired using software developed by J. Brown (University of Miami), and the

in-water data were processed by S. Maritorena (University of California at Santa Barbara). Both persons have repeatedly contributed to the success of various components of the SeaWiFS field campaigns, and their initiative is greatly appreciated. Part of the above-water dataset was processed by G. Lazin (Satlantic, Inc.) who also provided helpful comments on an early draft of the results. The *Q*-factor corrections were provided by B. Gentili (Université Pierre et Marie Curie), and his assistance was indispensable. J. Mueller is thanked for many useful and insightful review comments, which improved the quality of the final manuscript. The final preparation of the manuscript benefitted from the editorial and logistical assistance of E. Firestone.

APPENDIX A

Glossary

IOCCG	International Ocean-Color Coordinating Group
JGOFS	Joint Global Ocean Flux Study
LoCNESS	Low-Cost NASA Environmental Sampling System
NASA	National Aeronautics and Space Administration
NPD	Net percent difference
PROSOPE	*Productivité des Systèmes Océaniques Pélagiques* (productivity of pelagic oceanic systems)
RPD	Relative percent difference
SDY	Sequential day of the year
SeaBOARR	SeaWiFS Bio-Optical Algorithm Round-Robin
SeaFALLS	SeaWiFS Free-Falling Advanced Light Level Sensors
SeaSAS	SeaWiFS Surface Acquisition System
SeaWiFS	Sea-viewing Wide Field-of-view Sensor
UPD	Unbiased percent difference

APPENDIX B

Primary Symbols

$E_d(\lambda, 0^+)$	The total solar irradiance just above the sea surface
$L_{\text{sky}}(\lambda)$	The sky radiance reaching the sea surface
$L_T(\lambda)$	The total spectral radiance immediately above the sea surface; see (5) and (15)
$L_u(\lambda)$	The spectral upwelled radiance; see (2)
$L_W(\lambda)$	The spectral water-leaving radiance; see (1), (3), (3′), (9), and (10)
$L_W^{\text{abw}}(\lambda)$	The spectral water-leaving radiance computed from above-water optical data
$L_W^{\text{inw}}(\lambda)$	The spectral water-leaving radiance computed from in-water optical data
$L_W^{\text{LN}}(\lambda)$	The spectral water-leaving radiance computed from (in-water) LoCNESS optical data
$L_W^{\text{M80}}(\lambda)$	The spectral water-leaving radiance computed using the Morel (1980) method; see (9)
$L_W^{\text{S95}}(\lambda)$	The spectral water-leaving radiance computed using the SeaWiFS Ocean Optics Protocols method (Mueller and Austin 1995 and as revised by Mueller et al. 2000); see (10)
$L_W^{\text{SF}}(\lambda)$	The spectral water-leaving radiance computed from (in-water) SeaFALLS optical data
$Q(\lambda)$	The spectral bidirectional *Q*-function; see (4); $Q_n(\lambda)$ denotes the *Q*-function at the nadir viewing angle
$r(865)$	A diagnostic variable for determining the amount of reflected (contamination) radiation at the sea surface; see (13)
$R_{\text{rs}}(\lambda)$	The spectral remote sensing reflectance; see (7) and (8)
$R_{\text{rs}}^{\text{S95}}(\lambda)$	The spectral remote sensing reflectance calculated using the S95 method to derive the water-leaving radiance
$T(\theta')$	The upward radiance transmittance through the sea surface; T_0 denotes a constant value for $T(\theta')$ when $\theta' = 0$ (equal to 0.546)
α_s	The amidships pointing angle of the SeaSAS instruments; see Fig. 4 (inset panel)
β_s	The angle between the radiometer and the swell direction; see Fig. 4 (inset panel)
γ_s	The angle between the center line of the ship and the position of the sun; see Fig. 4 (inset panel)
$\delta_B^A(\lambda_i)$	The RPD at center wavelength (channel) λ_i for two data products $L_W^A(\lambda_i)$ and $L_W^B(\lambda_i)$, where the *A* and *B* codes identify the methods or data sources used; see (12)
$\overline{\delta}_B^A(\lambda_i)$	The average of δ_B^A over *N* casts
ΔL	A contaminating radiance contribution; see (5)
$\Delta L_{\text{ship}}(\lambda)$	The ship perturbation radiance contribution to the above-water radiance field; see (14), (15), and (16)
θ	The zenith angle
θ'	The nadir angle
θ_s	The solar zenith angle
λ_r	A wavelength or channel in the near-infrared part of the spectrum
ϕ	The azimuth angle with respect to the sun direction ($\phi = 0$ for the sun's azimuth)
ρ	The Fresnel reflectance coefficient
$\psi_B^A(\lambda_i)$	The UPD at center wavelength (channel) λ_i for two data products $L_W^A(\lambda_i)$ and $L_W^B(\lambda_i)$, where the *A* and *B* codes identify the methods or data sources used; see (11)

REFERENCES

Austin, R. W., 1974: The remote sensing of spectral radiance from below the ocean surface. *Optical Aspects of Oceanography,* N. G. Jerlov and E. S. Nielsen, Eds., Academic Press, 317–344.

Fougnie, B., P-Y. Deschamp, and R. Frouin, 1999: Vicarious calibration of the POLDER ocean color spectral bands using *in situ* measurements. *Trans. IEEE Trans. Geosci. Remote Sens.,* **37,** 1567–1574.

Gordon, H. R., 1985: Ship perturbation of irradiance measurements at sea. 1: Monte Carlo simulations. *Appl. Opt.,* **24,** 4172–4182.

Hooker, S. B., and W. E. Esaias, 1993: An overview of the SeaWiFS project. *EOS Trans. Amer. Geophys. Union,* **74,** 241–246.

——, and J. Aiken, 1998: Calibration evaluation and radiometric testing of field radiometers with the SeaWiFS Quality Monitor (SQM). *J. Atmos. Oceanic Technol.,* **15,** 995–1007.

——, and G. Lazin, 2000: The SeaBOARR-99 Field Campaign. NASA Tech. Memo. 2000-206892, Vol. 8, S. B. Hooker and E. R. Firestone, Eds., NASA Goddard Space Flight Center, Greenbelt, Maryland, 46 pp.

——, and S. Maritorena, 2000: An evaluation of oceanographic radiometers and deployment methodologies. *J. Atmos. Oceanic Technol.,* **17,** 811–830.

——, and C. R. McClain, 2000: The Calibration and Validation of SeaWiFS Data. *Progress in Oceanography,* Vol. 45, Pergamon, 427–465.

——, G. Zibordi, G. Lazin, and S. McLean, 1999: The SeaBOARR-98 Field Campaign. NASA Tech. Memo. 1999-206892, Vol. 3, S. B. Hooker and E. R. Firestone, Eds., NASA Goddard Space Flight Center, Greenbelt, Maryland, 40 pp.

——, ——, J-F. Berthon, D. D'Alimonte, S. Maritorena, S. McLean, and J. Sildam, 2001: Results of the Second SeaWiFS Data Analysis Round Robin, March 2000 (DARR-00). NASA Tech. Memo. 2001-206892, Vol. 15, S. B. Hooker and E. R. Firestone, Eds., NASA Goddard Space Flight Center, Greenbelt, Maryland, 71 pp.

——, G. Lazin, G. Zibordi, and S. McLean, 2002a: An evaluation of above- and in-water methods for determining water-leaving radiances. *J. Atmos. Oceanic Technol.,* **19,** 486–515.

——, S. McLean, J. Sherman, M. Small, G. Zibordi, and J. Brown, 2002b: The Seventh SeaWiFS Intercalibration Round-Robin Experiment (SIRREX-7), March 1999. NASA Tech. Memo. 2002-206892, Vol. 17, S. B. Hooker and E. R. Firestone, Eds., NASA Goddard Space Flight Center, Greenbelt, Maryland, 69 pp.

IOCCG, 1998: Minimum requirements for an operational ocean-colour sensor for the open ocean. International Ocean-Colour Coordinating Group Rep. 1, IOCCG, Nova Scotia, Canada, 46 pp.

Loisel, H., and A. Morel, 1998: Light scattering and chlorophyll concentration in case 1 waters: A reexamination. *Limnol. Oceanogr.,* **43,** 847–858.

Mobley, C. D., 1999: Estimation of the remote-sensing reflectance from above-surface measurements. *Appl. Opt.,* **38,** 7442–7455.

Morel, A., 1980: In-water and remote measurements of ocean color. *Bound.-Layer Meteor.,* **18,** 177–201.

——, and B. Gentili, 1996: Diffuse reflectance of oceanic waters, III. Implication of bidirectionality for the remote sensing problem. *Appl. Opt.,* **35,** 4850–4862.

Mueller, J. L., 2000a: Overview of measurement and data analysis protocols. NASA Tech. Memo. 2000-209966, Ocean Optics Protocols for Satellite Ocean Color Sensor Validation, Revision 2, G. S. Fargion, and J. L. Mueller, Eds., NASA Goddard Space Flight Center, Greenbelt, Maryland, 65–86.

——, 2000b: In-water radiometric profile measurements and data analysis protocols. NASA Tech. Memo. 2000-209966, Ocean Optics Protocols for Satellite Ocean Color Sensor Validation, Revision 2, G. S. Fargion and J. L. Mueller, Eds., NASA Goddard Space Flight Center, Greenbelt, Maryland, 87–97.

——, and R. W. Austin, 1992: Ocean Optics Protocols for SeaWiFS Validation. NASA Tech. Memo. 104566, Vol. 5, S. B. Hooker and E. R. Firestone, Eds., NASA Goddard Space Flight Center, Greenbelt, Maryland, 43 pp.

——, and ——, 1995: Ocean Optics Protocols for SeaWiFS Validation, Revision 1. NASA Tech. Memo. 104566, Vol. 25, S. B. Hooker, E. R. Firestone, and J. G. Acker, Eds., NASA Goddard Space Flight Center, Greenbelt, Maryland, 66 pp.

——, and Coauthors, 2000: Above-water radiance and remote sensing reflectance measurement and analysis protocols. Ocean Optics Protocols for Satellite Ocean Color Sensor Validation, Revision 2. NASA Tech. Memo. 2000-209966, G. S. Fargion and J. L. Mueller, Eds., NASA Goddard Space Flight Center, Greenbelt, Maryland, 98–107.

O'Reilly, J. R., S. Maritorena, B. G. Mitchell, D. A. Siegel, K. L. Carder, S. A. Garver, M. Kahru, and C. McClain, 1998: Ocean color chlorophyll algorithms for SeaWiFS. *J. Geophys. Res.,* **103,** 24 937–24 953.

Siegel, D. A., M. H. Wang, S. Maritorena, and W. Robinson, 2000: Atmospheric correction of satellite ocean color imagery: The black pixel assumption. *Appl. Opt.,* **39,** 3582–3591.

Smith, R. C., and K. S. Baker, 1984: The analysis of ocean optical data. *Ocean Optics VII,* M. A. Blizard, Ed., Vol. 478, SPIE, 119–126.

Toole, D. A., D. A. Siegel, D. W. Menzies, M. J. Neumann, and R. C. Smith, 2000: Remote sensing reflectance determinations in the coastal ocean environment—Impact of instrumental characteristics and environmental variability. *Appl. Opt.,* **39,** 456–469.

Voss, K. J., J. W. Nolten, and G. D. Edwards, 1986: Ship shadow effects on apparent optical properties. *Ocean Optics XII,* J. S. Jaffe, Ed., Vol. 2258, SPIE, 815–821.

Weir, C. T., D. A. Siegel, A. F. Michaels, and D. W. Menzies, 1994: In situ evaluation of a ship's shadow. *Ocean Optics VIII,* M. A. Blizzard, Ed., Vol. 637, SPIE, 186–190.

Zaneveld, J. R. V., E. Boss, and A. Barnard, 2001: Influence of surface waves on measured and modeled irradiance profiles. *Appl. Opt.,* **40,** 1442–1449.

Zibordi, G., J. P. Doyle, and S. B. Hooker, 1999: Offshore tower shading effects on in-water optical measurements. *J. Atmos. Oceanic Technol.,* **16,** 1767–1779.